Steerable chiral optical responses unraveled in planar metasurfaces via bound states in the continuum

Qin-Ke Liu,[1] Yan Li,[2] Zhendong Lu,[1] Yaojie Zhou,[1] W. M. Liu,[3] Xiao-Qing Luo,[1,*] and Xin-Lin Wang[4,1]

[1]*School of Electrical Engineering, University of South China, Hengyang 421001, China*
[2]*School of Nuclear Science and Technology, University of South China, Hengyang 421001, China*
[3]*Beijing National Laboratory for Condensed Matter Physics, Institute of Physics, Chinese Academy of Sciences, Beijing 100190, China*
[4]*Hunan Province Key Laboratory for Ultra-Fast Micro/Nano Technology and Advanced Laser Manufacture, School of Mechanical Engineering, University of South China, Hengyang 421001, China*

(Received 28 June 2023; accepted 27 September 2023; published 10 October 2023)

Chiral metasurfaces, with appealing properties for studying light-matter interactions at the nanoscale, have emerged as a promising platform for the realization of chiral optical responses, thereby showing advantages in chirality-related applications. The conventional approaches primarily concentrate on circular dichroism and the high Q factor of the chiral resonances, while little attention has been paid to the aspects of flexibility and controllability in the modulation of optical chirality, further inhibiting the implementation of tunable and multifunctional chiral metadevices. Here, we employ a planar chiral silicon metasurface governed by bound states in the continuum (BICs) to unravel steerable chiral optical responses. In particular, the BIC-based intrinsic and extrinsic planar chiralities can be precisely steered by breaking the in-plane symmetry and the illumination symmetry, respectively. Moreover, a hybrid Si-VO_2 metasurface, manifested by the chiral coupled-mode theory, showcases the feasibility of actively tuning the dissipative loss while maintaining chiral quasi-BICs, then yielding desired loss-steered optical chirality. Our results provide alternative insights into tunable optical chirality and pave the way for advancements in chiroptical applications.

DOI: 10.1103/PhysRevB.108.155410

I. INTRODUCTION

Chirality refers to the property of an object in which it cannot be superimposed on its mirror image through rotations and translations [1–3]. It is well known that many natural objects can exhibit chirality, such as conch shells, DNA, and molecular structures. The study of chirality is of tremendous significance in scientific research fields, including analytical chemistry [4], nanomedicine [5], and the search for extraterrestrial life [6]. As chiral objects interact with light, a unique optical response termed the chiral optical response can be induced, characterizing the differences in intensity and phase between left-handed circularly polarized (LCP) and right-handed circularly polarized (RCP) light illuminations and emerging circular dichroism (CD), chiral field enhancement, and so on [7,8]. However, in many natural chiral materials, the optical chirality is typically weak and challenging to control. Fortunately, with the remarkable advancements in nanoscience and nanotechnology, the development of optical chirality has experienced explosive growth. For instance, chiral metamaterials consisting of unit cells (meta-atoms) that employ chiral structural designs can empower chiroptical properties that are beyond the reach of natural objects [8–13]. Chiral metasurfaces that are two-dimensional metamaterials composed of periodic or aperiodic subwavelength artificial structures possess the capability of manipulating electromagnetic wave fronts, thus enabling the enhancement of optical chirality through fine control of materials and the unit cell geometric configuration [8,14–16]. Compared to chiral metamaterials, chiral metasurfaces that eliminate one degree of freedom associated with three-dimensional structures have been explored in pursuit of both intrinsic planar chirality at normal incidence [14,17,18] and extrinsic chirality at oblique incidences [10,19,20]. This reduction not only can simplify the fabrication process but also can provide good tolerance of fabrication imperfections. Therefore, owing to their flat, ultrathin, and compact nature, chiral metasurfaces have gained prominence in various applications, including biosensing [21–23], chiral harmonic generation [14,24–27], and chiral lasing [28,29].

In recent years, the emergence of bound states in the continuum (BICs) in photonics has provided a promising avenue for chiroptics [16,30–32]. BICs, which reside in the radiation continuum but are unaffected by damping, were initially proposed in the field of quantum mechanics [33] and have subsequently been demonstrated in various wave systems [34–36], particularly optics. These states have garnered significant attention due to their infinite-Q-factor property, offering new possibilities for photonics applications that require strong light-matter interactions. In practical applications, BICs often undergo transformations into radiative states that couple with free space as a result of small perturbations [35,37–41], yielding quasi-BIC (q-BIC) modes that can exhibit characteristics similar to supercavity modes. This fascinating physical property has been successfully harnessed in chiral metasurfaces,

---

[*] Corresponding author: xqluophys@gmail.com

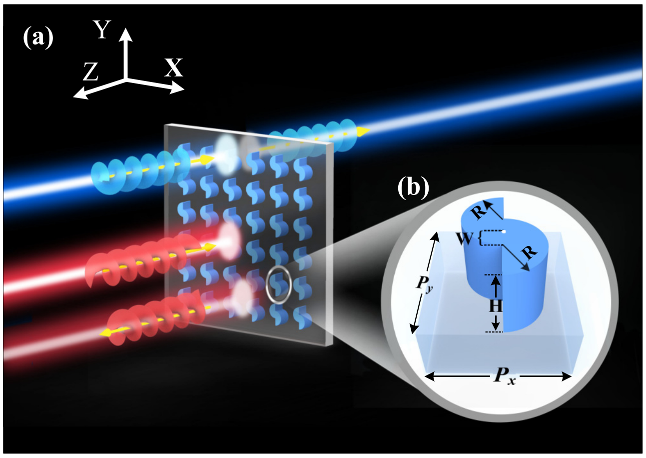

FIG. 1. (a) Schematic illustration of a planar silicon metasurface supported chiral BIC, which consists of double-semicircle unit cells deposited on a quartz substrate. The incident circularly polarized light acts vertically, along the negative-Z direction, on the metasurface. (b) Zoomed view and the related geometric parameters for the unit cell.

leading to the realization of ultrahigh Q factors and nearly perfect single chirality [14,16,42,43], expanding the repertoire of methods and applications for achieving optical chirality. However, conventional wisdom on chiral metasurfaces is primarily to unveil a perfect single CD and Q factors of chiral resonances, whereas few studies aim at the utility of flexibility and accessibility in optical chirality. This limitation also hinders the design and implementation of tunable and multifunctional chiral metadevices. Consequently, actively steering optical chirality while satisfying the requirements for the chirality intensity and Q factor is desired and still needs to be further explored.

In this paper, we theoretically propose and numerically demonstrate that a planar chiral silicon metasurface governed by BICs can be employed to unravel steerable chiral optical responses that enclose intrinsic and extrinsic planar chiralities. In particular, the intrinsic planar chirality can be accomplished by tailoring the in-plane symmetry at normal incidence, while the tunable extrinsic planar chirality can be implemented by altering the illumination symmetry at oblique incidence. Moreover, a hybrid Si-VO$_2$ metasurface is proposed to enable loss-steered chiral optical responses which is rationalized based on chiral coupled-mode theory and showcases the feasibility of actively tuning the temperature-dependent dissipative loss for achieving desired q-BIC sustained optical chirality. Our results offer an alternative approach for tunable optical chirality and show advantages in chiral metadevices.

II. STRUCTURE AND MODEL

Herein, we consider a planar silicon metasurface that consists of periodic silicon double-semicircle (DS) unit cells, as shown in Fig. 1(a), deposited on a quartz substrate. The circularly polarized light (CPL), including the LCP and RCP, propagates along the negative-Z direction and acts vertically on the metasurface. The related geometric parameters of the unit cell are presented in Fig. 1(b). $R = 200$ nm depicts the radii of the DS structure, with $W = 100$ nm being the distance between either of the semicircle centers and the unit cell center in the Y direction. $H = 350$ nm denotes the height of the DS structure. $P_x = P_y = 800$ nm are the periodic lengths of the unit cell in the X and Y directions, respectively. Moreover, the numerical simulation of the planar silicon metasurfaces can be achieved by harnessing the finite-element method, where the dielectric constants of silicon and quartz are from Palik's handbook, with the extinction coefficient κ of silicon at 1000–1200 nm being reduced from 4.90×10^{-4} to 1.39×10^{-7} [44,45]. Therein, the perfectly matched layers are set as the boundary conditions on the front and back sides of the Z direction, which can enact a reflectionless absorbing medium that absorbs without any reflected electromagnetic waves at all frequencies and angles of incidence. The periodic boundary conditions that ensure the continuous distribution of media on the boundary are set in the X and Y directions of the planar silicon metasurface. In particular, the Floquet periodic boundary conditions are used in both the X and Y directions for oblique illuminations, and the eigenfrequency solver in COMSOL MULTIPHYSICS simulation software is used to compensate their phase differences and replicate an infinite planar array of the unit cell.

III. THE BAND STRUCTURE AND POLARIZATION MAPS NEAR THE Γ POINT

To characterize the physics of BICs with chiral properties, we study the eigenmodes of the planar silicon metasurface that are analyzed using the eigenfrequency solver (here, COMSOL MULTIPHYSICS). As shown in Figs. 2(a) and 2(b), the band structures of three modes (the related wavelengths are from 1025 to 1085 nm) and their quality factors (Q factors) present at the first Brillouin zone (near the Γ point) along the M-Γ-X direction, respectively. Among them, mode 3 (orange solid line) shows the characteristics of ideal symmetry-protected BIC [37,46], thus leading to the Q factor at the Γ point tending to infinity, where the considered silicon is without the intrinsic loss. However, as shown in Fig. 2(d), the eigenpolarization map elucidates that the at Γ the BIC occurs as a vortex polarization singularity (V point, labeled as a black dot), which is defined by the Poincaré sphere axes as $(S_0, S_1, S_2, S_3 = 0)$ [31,47]. It has been demonstrated that fine-tuning the geometric asymmetry of the unit cell can indicate the presence of intrinsic chirality of the related metasurface. By varying L of the DS structure and introducing the asymmetric parameter ΔS, the in-plane inversion C_2^z symmetry is broken, as shown in Fig. 2(c). In this way, $L = 10$ nm, and the V point is split into a pair of circularly polarized states (C points, marked as red and blue dots), defined as $(S_1, S_2 = 0)$, with opposite chiral properties in the proximity of the Γ point [31], as shown in Fig. 2(e). By further increasing to $L = 50$ nm, in Fig. 2(f), the C points move far away from the Γ point along one of the diagonal directions in k space. Consequently, the chiral BIC with adjustable C points in k space in the planar silicon metasurface holds the key to unlocking high-Q and tunable chiral optical responses.

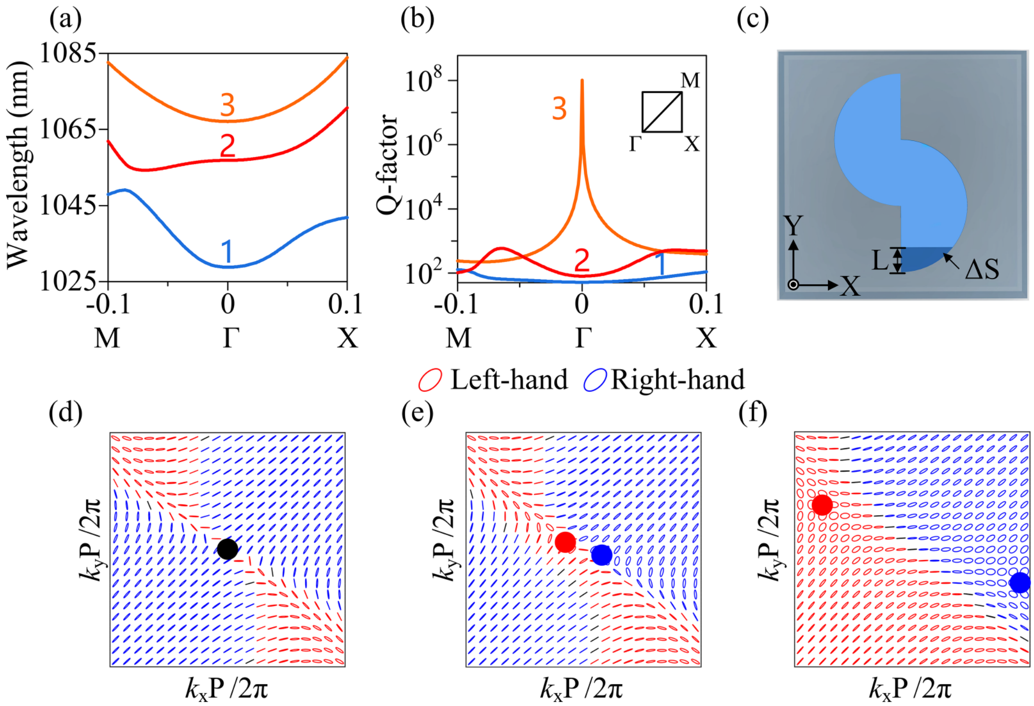

FIG. 2. The simulated band structure and Q factor of the related eigenmodes of the planar silicon metasurface near the Γ point, as well as eigenpolarization maps with different values of L. (a) and (b) The band structure and Q factor of the eigenmodes in the vicinity of the Γ point with $L = 0$ nm. (c) Top view of the unit cell suffering from in-plane geometry symmetry breaking that results from the asymmetric parameter ΔS. (d)–(f) Eigenpolarization maps, where the polarization states are represented by blue and red ellipses corresponding to left-handed and right-handed states in k space with $L = 0$ nm, $L = 10$ nm, and $L = 50$ nm, respectively.

IV. INTRINSIC PLANAR CHIRALITY EMPOWERED BY IN-PLANE SYMMETRY BREAKING

In the following, breaking the in-plane C_2^z symmetry of the DS structure, as depicted in Fig. 3(a), we study the intrinsic chiral q-BIC responses in planar silicon metasurface under normal incidence. It is found that the variation of the related structural parameters of the metasurface, yielding inversion symmetry breaking, makes the symmetry-protected BICs transform into chiral q-BICs. Figure 3(b) shows the transmittance Jones matrix spectra and the CD spectrum of the chiral q-BIC metasurface with in-plane C_2^z symmetry breaking ($L = 50$ nm). Therein, measured in the far field, the collective effect of the near-field chiral properties over the entire metasurface is defined as the transmittance difference under RCP and LCP incidences [14,16],

$$\mathrm{CD} = \frac{(T_{RR} + T_{LR}) - (T_{RL} + T_{LL})}{(T_{RR} + T_{LR}) + (T_{RL} + T_{LL})}, \qquad (1)$$

where L and R represent the LCP and RCP, respectively. T_{ij} $(i = L, R; j = L, R)$ denotes the transmittance of output polarization i from the input polarization j. As for the chiral q-BIC mode at 1062 nm, T_{RR} exhibits a sharp peak [see the red curve in Fig. 3(b)], whereas T_{RL} displays a dip near zero [see the orange curve in Fig. 3(b)], with T_{LL} immobilizing at zero [see the light blue curve in Fig. 3(b)]. Meanwhile, T_{LR} reveals a low dip, resulting in the realization of RCP → LCP (24.6%) polarization conversion [see the purple curve in Fig. 3(b)]. These indicate that an ultrasharp CD spectrum can be implemented with a maximum (>0.95) and an ultranarrow linewidth of 2.2 nm. Subsequently, the Cartesian multipole expansion (see the Appendix) of the far-field scattering cross section of the chiral q-BIC mode (under RCP normal incidence) [48] in Fig. 3(c) is dominated by the electric quadrupole (EQ), with the electric dipole being a secondary contribution. This behavior can also be validated by the electric field distribution (color) and magnetic fields H_x and H_y (vector) from the *silicon-quartz interface* of the chiral q-BIC mode governed by the EQ mode in Fig. 3(d). In Fig. 3(e), by varying L of the DS structure from $L = 0$ nm to $L = 100$ nm, the CD spectra evolve from a BIC (see the red circle) to a radiative chiral q-BIC with the linewidth increasing from zero to a finite value, sustaining near-unitary CD peaks values with finite linewidth. In addition, the Q factor of the chiral q-BIC modes in Fig. 3(f) is inversely proportional to the *in-plane asymmetric parameter* $\alpha = \Delta S/S$, which is in good agreement with α^{-2}, characterizing the ideal symmetry-protected q-BIC modes (without considering the loss of the silicon). As a consequence, the in-plane symmetry breaking of the DS metasurface can empower the occurrence of tailorable intrinsic planar chirality via chiral q-BIC responses.

V. EXTRINSIC PLANAR CHIRALITY ENABLED BY ILLUMINATION SYMMETRY BREAKING

With regard to the customizable intrinsic chiral responses, we can also access the tunable extrinsic chiral responses under oblique incidence. As illustrated in Fig. 4(a), the illumination symmetry breaking, namely, the out-of-plane mirror symmetry breaking, can be achieved by varying the incident

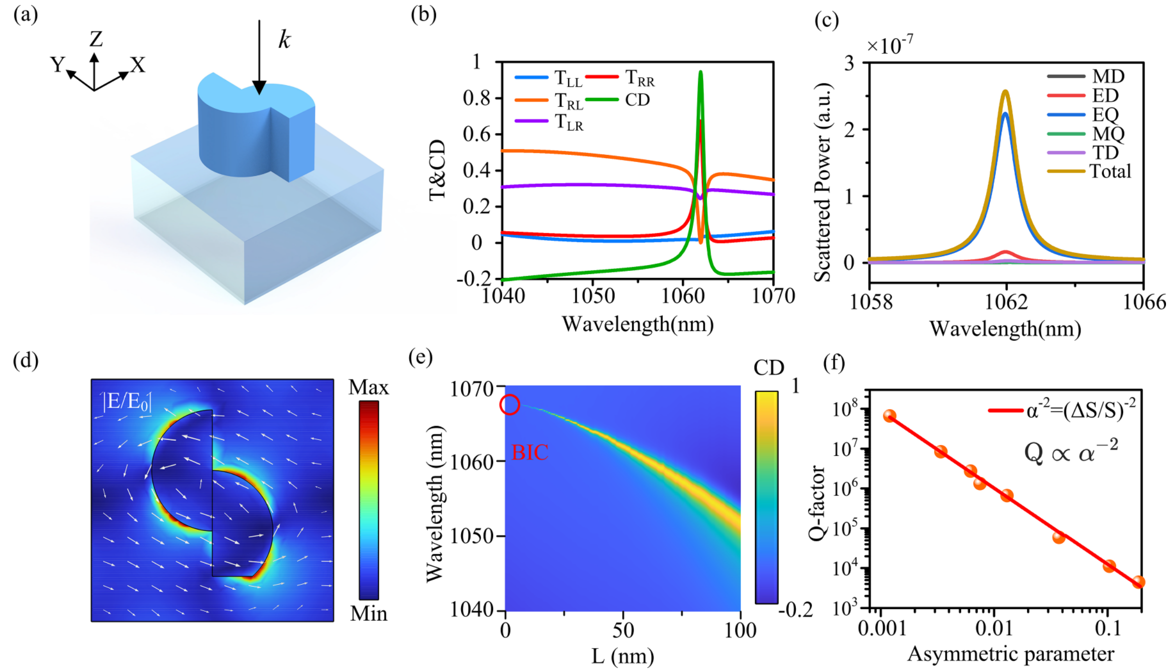

FIG. 3. (a) The side view of the unit cell in the planar silicon metasurface under normal incidence. (b) The transmittance Jones matrix spectra of T_{RR}, T_{RL}, T_{LR}, and T_{LL} and the CD spectrum of the chiral q-BIC metasurface with symmetry breaking ($L = 50$ nm). (c) The Cartesian multipole expansion of the scattering cross-section spectra of the chiral q-BIC mode in (b). (d) The electric field distribution (color) and magnetic fields H_x and H_y (vector) of the chiral q-BIC mode governed by the electric quadrupole. (e) The evolution of CD spectra by varying L. (f) Dependence of the Q factor of the chiral q-BIC modes on the in-plane asymmetric parameter $\Delta S/S$. The orange solid line exhibits an inverse quadratic fitting.

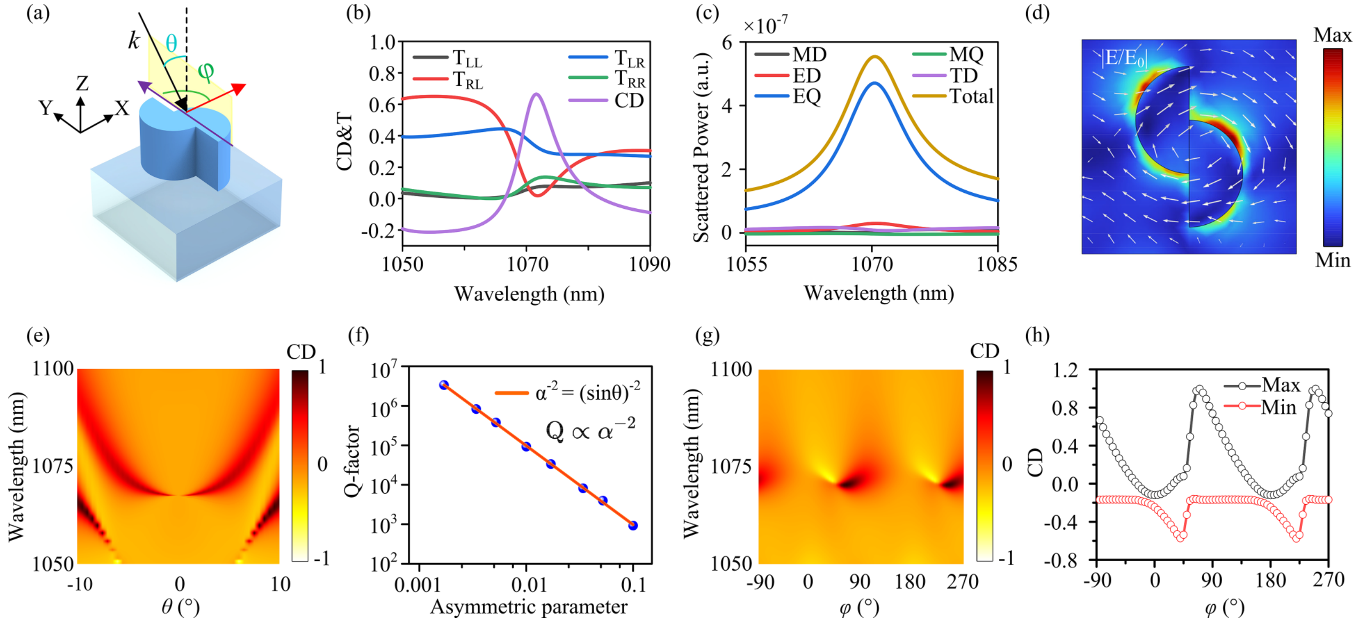

FIG. 4. (a) The side view of the unit cell in the planar silicon metasurface under oblique incidence. (b) The transmittance Jones matrix spectra and the CD spectrum of the chiral q-BIC metasurface. (c) The Cartesian multipole expansion of the scattering cross-section spectra of the chiral q-BIC mode in (b). (d) The electric field distribution (color) and magnetic fields H_x and H_y (vector) of the chiral q-BIC mode predominated by the EQ. (e) The evolution of the CD spectra as a function of θ. (f) The Q factor of the chiral q-BIC modes for the out-of-plane asymmetry parameter $\sin\theta$, with the orange solid line being an inverse quadratic fitting. With a fixed incident angle $\theta = 5°$, (g) the CD spectra versus the wavelength and the conical angle φ and (h) the related maximum and minimum of the CD spectra with respect to the conical angle φ.

angle θ along the Y direction with the conical angle $\varphi = 90^\circ$. Figure 4(b) elucidates the transmittance Jones matrix spectra and the CD spectrum of the chiral q-BIC metasurface with $\theta = 5^\circ$ and $\varphi = 90^\circ$. Regarding the chiral q-BIC mode at 1072 nm, one can see a sharp CD spectrum (peak value equals 0.67; see the purple curve) with a narrow linewidth of 9.8 nm. Moreover, T_{RL} denotes a dip near zero (see the red curve), and T_{LR} depicts a slight dip, giving rise to the appearance of the RCP → LCP (33.3%) polarization conversion (see the blue curve). Conversely, T_{LL} and T_{RR} delineate a single peak next to 0.05 (see the black and green curves), respectively. In addition, the extrinsic chiral q-BIC mode in the Cartesian multipole expansion (see the Appendix) in Fig. 4(c) is predominated by the EQ. This behavior can also be identified from the electromagnetic field distribution in Fig. 4(d), where the related distribution is from the *silicon-quartz interface*. Figure 4(e) illustrates the evolution of the CD spectra by continuously varying the incident angle θ from -10° to 10° along the Y direction ($\varphi = 90^\circ$). The linewidth of the CD peak decreases from finite values to zero as the incident angle θ tends to 0°, capturing the transfer process from radiative q-BIC modes to a nonradiative BIC state with strong extrinsic chirality. The Q factors of the extrinsic chiral q-BIC modes in Fig. 4(f) are also obviously inverse quadratic versus the *out-of-plane asymmetric parameter* $\alpha = \sin\theta$. It is of great interest to see that, in Fig. 4(g), the evolution of CD spectra with varying conical angles φ and a fixed incident angle $\theta = 5^\circ$ unfolds the different signs of the CD owing to the opposite helicities of the eigenpolarization sustained by the DS structure along the X and Y directions. Furthermore, for the maximum and minimum of the CD spectra in Fig. 4(h), it is obvious that the sign flip of the CD can be fulfilled (the maximum and minimum are > 0.99 and -0.582, respectively), uncovering periodic dependence (180°) on the conical angle φ. This implies that, by varying the incident angle θ and the conical angle φ of the incident light, the tunable extrinsic planar chirality can be realized by manipulating the illumination symmetry breaking.

VI. LOSS-STEERED CHIRAL OPTICAL RESPONSES VIA BOUND STATES IN THE CONTINUUM

With the consideration of the optical chirality, the intrinsic chirality can be customized with the adjustment of the structural parameters of the metasurface but is difficult to change flexibly, whereas the illumination symmetry breaking can be manipulated for tunable extrinsic chirality, requiring precise adjustment of the incident angle and conical angle. It has been proved that the maximum chirality can be achieved with the loss of the chiral BIC metasurfaces [16]. Thus, the regulable loss of such metasurfaces is highly desirable to have the ability to actively steer the optical chirality. Phase change materials, such as chalcogenide glass ($Ge_2Sb_2Te_5$, nonvolatile) and vanadium dioxide (VO_2, volatile), can exhibit large changes in their complex refractive index owing to the reversible phase transition triggered by an external (electrical, thermal, or optical) excitation [49,50]. It is noteworthy that the reversible phase transition in VO_2 appears near room temperature, which makes it a promising candidate for realizing tunable metadevices [51–54].

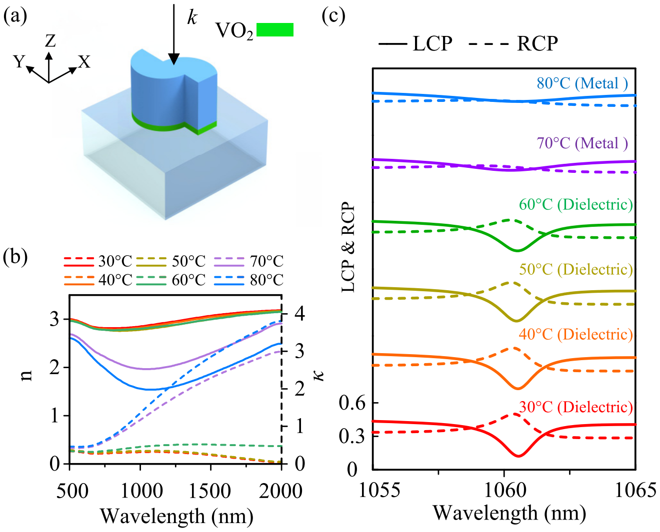

FIG. 5. (a) Sketch of the hybrid Si-VO_2 metasurface. (b) Refractive index of VO_2 with different temperatures from 500 to 2000 nm. (c) Transmittance of LCP and RCP by altering the temperatures.

In this context, we design a hybrid Si-VO_2 DS metasurface with tunable optical chirality with VO_2 (h is the height of VO_2 film, herein, $h = 5$ nm) located between the DS structure and quartz substrate, as shown in Fig. 5(a). Experimentally, the VO_2 thin film can be fabricated by chemical vapor deposition, pulsed laser deposition, sputtering, atomic layer deposition, and the chemical solution method [53,54]. As the reversible phase transition in VO_2 is about 68 °C, a dielectric state presents below the phase transition temperature, while a metallic state occurs above the phase transition temperature. The real and imaginary parts of the refractive index of vanadium dioxide with different temperatures (500 to 2000 nm) were taken from Ref. [55], as shown in Fig. 5(b). In particular, the contrast of the real part of the refractive index between 30 °C and 80 °C is $\Delta n \approx 1.33$ at 1060 nm, whereas the contrast of the imaginary part is $\Delta\kappa \approx 1.21$. As for the dielectric states of VO_2 (i.e., the temperatures range from 30 °C to 60 °C), as depicted in Fig. 5(c), the transmittance of LCP (RCP) exhibits a dip (peak), which decreases with increasing temperatures as a result of the slight increase of the extinction coefficient κ of VO_2. Note that the peak in the LCP resonance and the dip in the RCP resonance are positioned at different wavelengths. By further increasing the temperature to 70 °C or 80 °C, VO_2 operates in the metallic state, presenting the flat transmittance of the LCP and RCP, which originates from the strong increase in the extinction coefficient κ of VO_2. Compared to the CD of the optical chirality, the chiral optical responses of the hybrid Si-VO_2 DS metasurface are mainly enforced by the transmittance difference of the RCP and LCP at normal incidence.

To elucidate the effect of loss on the chiral optical responses, coupled-mode theory (CMT), which allows the expression of abstract scattering amplitudes in terms of physically meaningful parameters, seems to be an effective approach to reproduce the optical chirality and clarify its underlying physical mechanism [16,43,56]. It is well known that the S-matrix equation can, in general, provide an efficacious description of the transmission and reflection of the light field interaction with the metasurfaces. For the related chiral optical responses, vector **b**, enclosing four amplitudes of the outgoing light fields, can be expressed in a linear relation with vector **a**, with four amplitudes of the LCP and RCP light fields incident on different ports (i.e., $\mathbb{I}$ and $\mathbb{II}$) of the metasurface. Then, the S-matrix equation in the circular polarization basis can be written as

$$\begin{pmatrix} b_{\mathrm{L}}^{\mathbb{I}} \\ b_{\mathrm{L}}^{\mathbb{II}} \\ b_{\mathrm{R}}^{\mathbb{I}} \\ b_{\mathrm{R}}^{\mathbb{II}} \end{pmatrix} = \begin{pmatrix} r_{\mathrm{LL}}^{\mathbb{I}} & t_{\mathrm{LL}}^{\mathbb{II}} & r_{\mathrm{LR}}^{\mathbb{I}} & t_{\mathrm{LR}}^{\mathbb{II}} \\ t_{\mathrm{LL}}^{\mathbb{I}} & r_{\mathrm{LL}}^{\mathbb{II}} & t_{\mathrm{LR}}^{\mathbb{I}} & r_{\mathrm{LR}}^{\mathbb{II}} \\ r_{\mathrm{RL}}^{\mathbb{I}} & t_{\mathrm{RL}}^{\mathbb{II}} & r_{\mathrm{RR}}^{\mathbb{I}} & t_{\mathrm{RR}}^{\mathbb{II}} \\ t_{\mathrm{RL}}^{\mathbb{I}} & r_{\mathrm{RL}}^{\mathbb{II}} & t_{\mathrm{RR}}^{\mathbb{I}} & r_{\mathrm{RR}}^{\mathbb{II}} \end{pmatrix} \begin{pmatrix} a_{\mathrm{L}}^{\mathbb{I}} \\ a_{\mathrm{L}}^{\mathbb{II}} \\ a_{\mathrm{R}}^{\mathbb{I}} \\ a_{\mathrm{R}}^{\mathbb{II}} \end{pmatrix}, \tag{2}$$

where r and t represent the amplitudes of the reflection and transmission, respectively. Meanwhile, the subscripts depict the final and initial circularly polarized states, where subscripts with the same and different letters correspond to copolarized and cross-polarized components, respectively.

To describe the interaction of the metasurface with the incoming light fields oscillating with a real frequency ω, the eigenstates can be derived using amplitudes slowly varying with the vector **M**, which indicates the eigenstate coupling to the corresponding circularly polarized light fields incident on different sides of the metasurface. c_{L} and c_{R} are the slowly varying amplitudes of the metasurface eigenstates, where the vector of these amplitudes $\mathbf{c} = (c_{\mathrm{L}}, c_{\mathrm{R}})^T$. Then, the circularly polarized light field can be described as

$$\frac{dc}{dt} = [i(\omega - \omega_0) - \gamma_0]c + \mathbf{M} \cdot \mathbf{a}, \tag{3}$$

with

$$\mathbf{M} = \begin{pmatrix} m_{\mathrm{L}}^{\mathbb{I}} & m_{\mathrm{L}}^{\mathbb{II}} & m_{\mathrm{R}}^{\mathbb{I}} & m_{\mathrm{R}}^{\mathbb{II}} \end{pmatrix} \tag{4}$$

denoting the coupling of the incident light fields with the eigenmodes. As such, the irradiation of the outgoing light fields can be described by another CMT equation,

$$\mathbf{b} = \mathbf{N}^{\mathrm{T}} \cdot \mathbf{c} + \mathbf{B} \cdot \mathbf{a}, \tag{5}$$

where the vector of outgoing light field amplitudes **b** is the same as on the left-hand side of Eq. (2), with the matrix

$$\mathbf{N} = \begin{pmatrix} m_{\mathrm{R}}^{\mathbb{I}} & m_{\mathrm{R}}^{\mathbb{II}} & m_{\mathrm{L}}^{\mathbb{I}} & m_{\mathrm{L}}^{\mathbb{II}} \end{pmatrix} \tag{6}$$

describing the irradiation of circularly polarized light fields from the corresponding sides of the metasurface, the components of which are related to Eq. (4) by Lorentz reciprocity. The second term on the right-hand side of Eq. (5) represents the background transmission. In this way, the related matrix of the background transmission **B** with dissipation can be given as

$$\mathbf{B} = \begin{pmatrix} \rho_{\mathrm{LL}}^{\mathbb{I}} & \tau_{\mathrm{LL}}^{\mathbb{II}} & \rho_{\mathrm{LR}}^{\mathbb{I}} & \tau_{\mathrm{LR}}^{\mathbb{II}} \\ \tau_{\mathrm{LL}}^{\mathbb{I}} & \rho_{\mathrm{LL}}^{\mathbb{II}} & \tau_{\mathrm{LR}}^{\mathbb{I}} & \rho_{\mathrm{LR}}^{\mathbb{II}} \\ \rho_{\mathrm{RL}}^{\mathbb{I}} & \tau_{\mathrm{RL}}^{\mathbb{II}} & \rho_{\mathrm{RR}}^{\mathbb{I}} & \tau_{\mathrm{RR}}^{\mathbb{II}} \\ \tau_{\mathrm{RL}}^{\mathbb{I}} & \rho_{\mathrm{RL}}^{\mathbb{II}} & \tau_{\mathrm{RR}}^{\mathbb{I}} & \rho_{\mathrm{RR}}^{\mathbb{II}} \end{pmatrix}. \tag{7}$$

The S matrix from Eq. (2), dominated by the stationary state of Eqs. (3) and (5), can be written as

$$\mathbf{S} = \mathbf{B} - \frac{\mathbf{N}^{\mathrm{T}} \cdot \mathbf{M}}{i(\omega - \omega_0) - \gamma_0}, \tag{8}$$

where $\gamma_0 = \gamma_r + \gamma_d$, with γ_r and γ_d being the radiative and dissipative parts of the eigenmodes, respectively. Afterward, the amplitudes of $t_{LR}^{\mathbb{I}}$, $t_{RR}^{\mathbb{I}}$, $t_{LL}^{\mathbb{I}}$, and $t_{RL}^{\mathbb{I}}$ from the S matrix in Eq. (8) can be described as

$$t_{LR}^{\mathbb{I}} = \tau_{LR}^{\mathbb{I}} - \frac{m_{\mathrm{R}}^{\mathbb{II}} m_{\mathrm{R}}^{\mathbb{I}}}{i(\omega - \omega_0) - \gamma_0}, \tag{9a}$$

$$t_{RR}^{\mathbb{I}} = \tau_{RR}^{\mathbb{I}} - \frac{m_{\mathrm{L}}^{\mathbb{II}} m_{\mathrm{R}}^{\mathbb{I}}}{i(\omega - \omega_0) - \gamma_0}, \tag{9b}$$

$$t_{LL}^{\mathbb{I}} = \tau_{LL}^{\mathbb{I}} - \frac{m_{\mathrm{R}}^{\mathbb{II}} m_{\mathrm{L}}^{\mathbb{I}}}{i(\omega - \omega_0) - \gamma_0}, \tag{9c}$$

$$t_{RL}^{\mathbb{I}} = \tau_{RL}^{\mathbb{I}} - \frac{m_{\mathrm{L}}^{\mathbb{II}} m_{\mathrm{L}}^{\mathbb{I}}}{i(\omega - \omega_0) - \gamma_0}, \tag{9d}$$

where $\tau_{ij}^{\mathbb{I}}$ $(i = L, R; j = L, R)$ denotes the amplitude of the background transmission and ω_0 is the resonance frequency. $m_{L(R)}^{\mathbb{I}}$ depict the parameters of the coupling between the eigenstates and the light fields of corresponding helicity incident on side $\mathbb{I}$ of the metasurface, while $m_{L(R)}^{\mathbb{II}}$ describe those for side $\mathbb{II}$.

It has been demonstrated that the CD can be realized by enhancing $|t_R|$ and, especially, suppressing $|t_L|$ [16,43]. By setting $\omega = \omega_0$, i.e., the on-resonance case, $|t_L|$ can be given as

$$\begin{aligned} \left|t_L^{\mathbb{I}}\right|^2 &= \left|t_{RL}^{\mathbb{I}}\right|^2 + \left|t_{LL}^{\mathbb{I}}\right|^2 \\ &= \left|\tau_{RL}^{\mathbb{I}} + \frac{m_{\mathrm{L}}^{\mathbb{II}} m_{\mathrm{L}}^{\mathbb{I}}}{\gamma_r + \gamma_d}\right|^2 + \left|\tau_{LL}^{\mathbb{I}} + \frac{m_{\mathrm{R}}^{\mathbb{II}} m_{\mathrm{L}}^{\mathbb{I}}}{\gamma_r + \gamma_d}\right|^2. \end{aligned} \tag{10}$$

This means that the optical chirality is rather sensitive to dissipative loss γ_d of the Si-VO$_2$ metasurface, which is much greater than the radiative part γ_r and is positively correlated with the extinction coefficient (the imaginary part of the refractive index κ) of such a metasurface, $\gamma_d \propto \kappa$ [16]. The signs of $m_{\mathrm{L}}^{\mathbb{I}}$, $m_{\mathrm{L}}^{\mathbb{II}}$, and $m_{\mathrm{L}}^{\mathbb{I}}$ can give rise to the modulation of CD.

Next, we study the loss-steered optical chirality of hybrid Si-VO$_2$ chiral q-BIC metasurfaces undergoing in-plane symmetry breaking at different temperatures. Figure 6(a) clearly shows that, at a temperature of 30 °C, with the VO$_2$ operating in the dielectric state, the hybrid metasurface exhibits a CD peak (purple curve, 0.63) and a sharp linewidth of 4.7 nm at 1060.5 nm. T_{LR} presents a shallow dip (blue curve), with T_{LL} being near zero. T_{RL} reveals a deepened dip (red curve) and suppresses the LCP → RCP polarization conversion, while T_{RR} shows a sharp peak (green curve). At 60 °C, a similar conclusion can be made, but the dip of T_{RL} [see the red curve in Fig. 6(b)] gets shallower with the enhancement of the polarization conversion, whereas the peak of T_{RR} decreases slightly [see the green curve in Fig. 6(b)], which is mainly ascribed to the increase in the extinction coefficient κ of VO$_2$. By further increasing the temperature to 80 °C, which is above the phase transition temperature (68°C), as shown

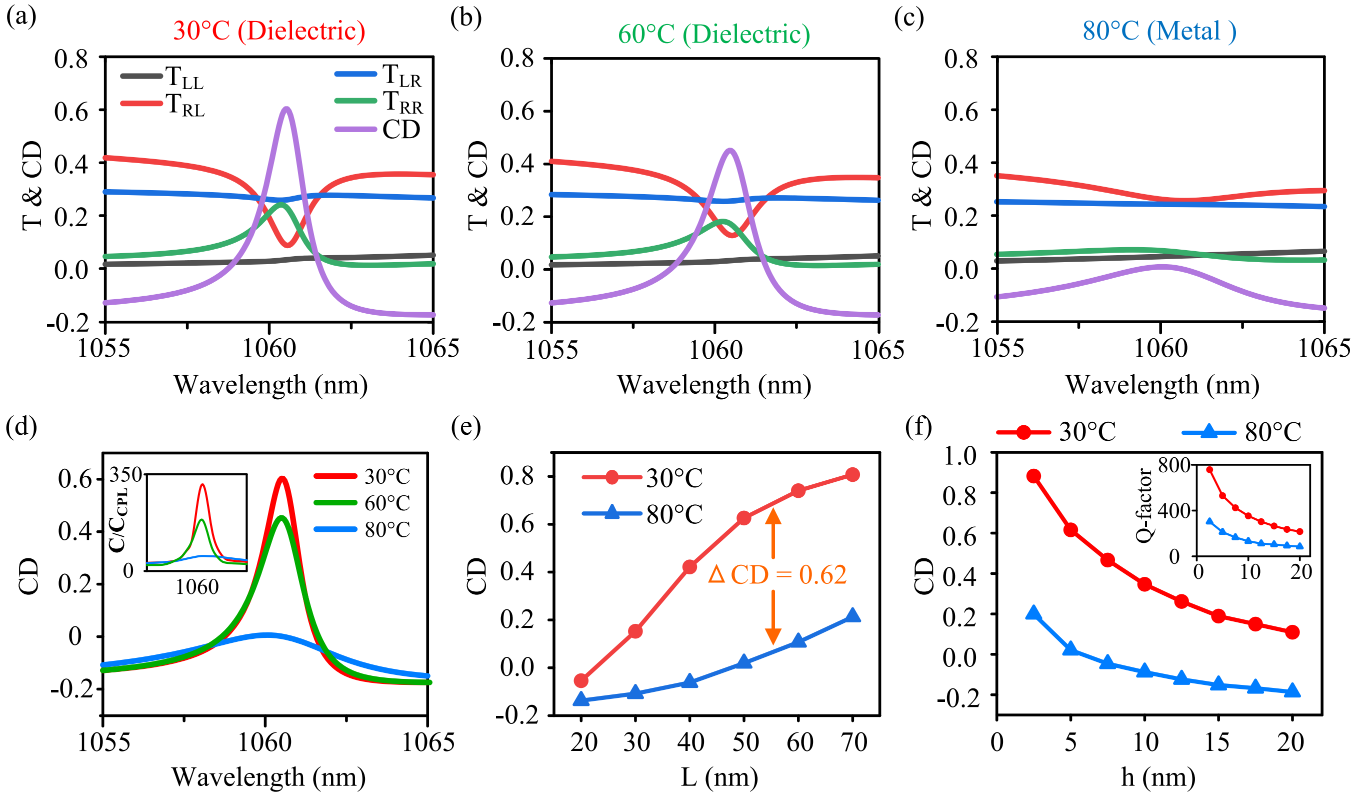

FIG. 6. (a)–(c) The Jones matrix spectra of T_{LL}, T_{RR}, T_{RL}, and T_{LR} and the CD spectrum of the actively steerable chiral q-BIC metasurface suffering from symmetry breaking ($L = 50$ nm) for different temperatures. (d) The CD spectrum and chiral enhancement (inset) of the actively steerable chiral q-BIC metasurface for different temperatures. (e) and (f) The CD spectra versus L and the height h of the VO_2 thin film, respectively, for different temperatures. The inset in (f) is the Q factor as a function of h at different temperatures.

in Fig. 6(c), T_{RR} is nearly gone (green curve), whereas T_{RL} is significantly enhanced, with the polarization conversion being 30% (red curve). Simultaneously, as shown in Fig. 6(d), the CD spectra of the three temperatures decrease successively near 1060.5 nm as the temperature increases from 30 °C to 80 °C. Here, the CD, which decreases from 0.63 (red curve) to 0.008 (blue curve), indicates the occurrence of a temperature-dependent chiral switching in the hybrid Si-VO_2 metasurface, allowing for the realization of operational characteristics that can be switched among left-handed, right-handed, and achiral states. Moreover, it is worth noting that a CD background spectrum of -0.2 enables the modulation of the CD down to zero or less by increasing the dissipative loss γ_d. Furthermore, the structural parameter L and the thickness h of the VO_2 thin film may have an obvious impact on the CD spectra of the hybrid Si-VO_2 metasurface. Additionally, as for the electromagnetic density of the chirality, $C = -\varepsilon_0 \omega \, \mathrm{Im}(\boldsymbol{E}^* \cdot \boldsymbol{B})/2$, where $\boldsymbol{E}^*$ and $\boldsymbol{B}$ denote the complex electric and magnetic fields and ω and ε_0 depict the angular frequency of light and the permittivity of free space, respectively. With respect to CPL in a vacuum, $C_{\mathrm{CPL}} = \pm \frac{\varepsilon_0 \omega}{2c} E_0^2$, with E_0 being the magnitude of the incident electric field. Thus, the chiral enhancement C/C_{CPL}, which represents the spatial maximum in C around the outside of a silicon metasurface, is achieved in the inset of Fig. 6(d) [57,58]. By varying the dissipative loss γ_d, a similar conclusion can be made about the chiral enhancement C/C_{CPL}. As depicted in Fig. 6(e), by varying L from 20 to 70 nm and keeping h at 5 nm for the hybrid Si-VO_2 metasurface, the CD spectra first increase and then saturate to a fixed value when the temperature is 30 °C (red curve with circles) but almost linearly increase when the temperature is 80 °C (blue curve with triangles). Notably, the maximal value of the CD difference ΔCD can be achieved near $L = 50$ nm. By referring to Eq. (10), it can be deduced that the same dissipative loss γ_d has a distinct effect on the $|t_L^{\mathbb{I}}|^2$ due to the different values of γ_r, $m_{L(R)}^{\mathbb{I}(\mathbb{II})}$, and $\tau_{ij}^{\mathbb{I}}$. In analogy to Fig. 3(f), the Q factor of the hybrid metasurface also exhibits a negative correlation with L. Moreover, with L fixed at 50 nm, the CD spectra in Fig. 6(f) exponentially decrease with the increase in the thickness h (from 2 to 20 nm) for temperatures of 30 °C (red curve with circles) and 80 °C (blue curve with triangles). The Q factor reveals a positive correlation with h, as shown in the inset of Fig. 6(f). These behaviors that arise from the increase in the film thickness h can be attributed to the variation of the dissipative loss γ_d, which resembles the method of suppression of temperature-dependent optical chirality. In addition, with respect to the extrinsic chirality at oblique incidence, the variation of the dissipative loss can also be exploited to achieve the desired optical chirality at low Q factors. Furthermore, for schemes similar to ours for incorporating dissipative loss from VO_2, it seems possible to extend our results by replacing VO_2 with other phase change materials [59–61], two-dimensional materials [40,61], etc. Accordingly, loss-steered chiral optical responses can be realized by manipulating the temperatures and related structural parameters of the hybrid Si-VO$_2$ metasurface.

VII. CONCLUSIONS

In summary, we have investigated steerable BIC-based chiral optical responses in planar metasurfaces that encompass silicon and hybrid Si-VO$_2$ double-semicircle structures with C_2^z symmetry. Specifically, the realization of at-Γ BICs reveals the V point in k space. A chiral optical response governed by symmetry-protected BICs can be accomplished due to the occurrence of adjustable C points near the Γ point. Furthermore, it was shown that the tailorable intrinsic planar chirality stems from the in-plane symmetry breaking, while the tunable extrinsic planar chirality originates from the illumination symmetry breaking. These behaviors enable the transformation of BICs into chiral quasi-BIC states and thus allow for precise control of the optical chirality by adjusting the asymmetric parameter and the polarization orientation of the incident light. Then, a hybrid Si-VO$_2$ metasurface was designed to actualize loss-steered chiral optical responses via q-BICs and was confirmed by the chiral coupled-mode theory, which can be implemented by actively tuning the temperature-dependent dissipative loss and the related structural parameters of the metasurface. Our results provide a unique probe of tunable optical chirality and have potential for developing flexibility and accessibility in applications in chiroptical metadevices.

ACKNOWLEDGMENTS

X.-Q.L. acknowledges support by the National Natural Science Foundation of China (Grant No. 12104214). W.-M.L. acknowledges support by the National Key Research and Development Program of China under Grants No. 2021YFA1400900, No. 2021YFA0718300, and No. 2021YFA1402100, National Natural Science Foundation of China under Grants No. 61835013, No. 12174461, and No. 12234012, Space Application System of China Manned Space Program.

APPENDIX: THE CARTESIAN MULTIPOLE EXPANSION

The electromagnetic multipole expansion is used to analyze each moment and its contribution to far-field radiation. For multipole decomposition in the Cartesian coordinate system, the polar moments can usually be obtained by integrating the carrier density $\rho(\vec{r})$ or the current density $\vec{J}(\vec{r})$ inside the structural unit cell. And then the sum of the far-field scattering intensity of all polar moments can be calculated at a certain frequency, thus leading to the total far-field scattering power. By integrating either the charge density or current density within the unit cell of the metasurface, all the multipoles under Cartesian coordinates can be defined as [62]

$$\vec{P} = \frac{1}{i\omega}\int \vec{j}d^3r, \tag{A1}$$

$$\vec{M} = \frac{1}{2c}\int \vec{r}\times\vec{j}d^3r, \tag{A2}$$

$$\vec{T} = \frac{1}{10c}\int [(\vec{r}\cdot\vec{j})\vec{r} - 2r^2\vec{j}]d^3r, \tag{A3}$$

$$Q_{\alpha,\beta}^{(e)} = \frac{1}{i2\omega}\int \left[r_\alpha j_\beta + r_\beta j_\alpha - \frac{2}{3}(\vec{r}\cdot\vec{j})\delta_{\alpha,\beta}\right]d^3r, \tag{A4}$$

$$Q_{\alpha,\beta}^{(m)} = \frac{1}{3c}\int [(\vec{r}\times\vec{j})_\alpha r_\beta + [\vec{r}\times\vec{j}]_\beta r_\alpha]d^3r, \tag{A5}$$

$$I_P = \frac{2\omega^4}{3c^3}|\vec{P}|^2, \tag{A6}$$

$$I_M = \frac{2\omega^4}{3c^3}|\vec{M}|^2, \tag{A7}$$

$$I_T = \frac{2\omega^6}{3c^5}|\vec{T}|^2, \tag{A8}$$

$$I_{Q^{(e)}} = \frac{\omega^6}{5c^5}\Sigma\left|Q_{\alpha,\beta}^{(e)}\right|^2, \tag{A9}$$

$$I_{Q^{(m)}} = \frac{\omega^6}{40c^5}\Sigma\left|Q_{\alpha,\beta}^{(m)}\right|^2, \tag{A10}$$

where $\alpha, \beta = x, y$. The symbols $\vec{P}$, $\vec{M}$, $\vec{T}$, $Q_{(e)}$, and $Q_{(m)}$ represent the electric dipole, magnetic dipole, toroidal dipole, electric quadrupole, and magnetic quadrupole, respectively. In the numerical simulations, we took into account the current density $\mathbf{J} = i\omega\varepsilon_0(\tilde{\varepsilon}_r - 1)\mathbf{E}$, which contributes to the absorption within metasurface, where ω is the angular frequency, ε_0 is the permittivity in vacuum, and $\tilde{\varepsilon}_r$ is the complex relative permittivity. Since the effect of higher-order polar moments on far-field scattering is small and negligible, the far-field scattering case can be characterized by the contribution of the above polar moments. Thus, the total far-field scattering intensity is expressed as follows:

$$I_{\text{Total}} = \frac{2\omega^4}{3c^3}|\vec{P}|^2 + \frac{2\omega^4}{3c^3}|\vec{M}|^2 + \frac{4\omega^5}{3c^4}(\vec{P}\cdot\vec{T}) + \frac{2\omega^6}{3c^5}|\vec{T}|^2 + \frac{\omega^6}{5c^5}\sum\left|Q_{\alpha,\beta}^{(e)}\right|^2 + \frac{\omega^6}{40c^5}\sum\left|Q_{\alpha,\beta}^{(m)}\right|^2 + O\left(\frac{1}{c^5}\right). \tag{A11}$$

It should be noted that the third part of the Eq. (A11) can be viewed as a composition of the electric and toroidal dipoles, without far-field radiation, owing to the complete destructive interference of their similar radiation patterns.

---

[1] L. Kelvin, *The Molecular Tactics of a Crystal* (Clarendon Press, Oxford, 1894).

[2] G. P. Moss, Basic terminology of stereochemistry (IUPAC recommendations 1996), Pure Appl. Chem. **68**, 2193 (1996).

[3] C. Menzel, C. Rockstuhl, and F. Lederer, Advanced Jones calculus for the classification of periodic metamaterials, Phys. Rev. A **82**, 053811 (2010).

[4] G. T. Tucker, Chiral switching, Lancet **355**, 1085 (2000).

[5] J. Yeom, P. P. G. Guimaraes, H. M. Ahn, B.-K. Jung, Q. Hu, K. McHugh, M. J. Mitchell, C.-O. Yun, R. Langer, and A. Jaklenec, Chiral supraparticles for controllable nanomedicine, Adv. Mater. **32**, 1903878 (2020).

[6] D. P. Glavin, A. S. Burton, J. E. Elsila, J. C. Aponte, and J. P. Dworkin, The search for chiral asymmetry as a potential biosignature in our solar system, Chem. Rev. **120**, 4660 (2020).

[7] I. Fernandez-Corbaton, M. Fruhnert, and C. Rockstuhl, Objects of maximum electromagnetic chirality, Phys. Rev. X **6**, 031013 (2016).

[8] Y. Chen, W. Du, Q. Zhang, O. Ávalos-Ovando, J. Wu, Q.-H. Xu, N. Liu, H. Okamoto, A. O. Govorov, Q. Xiong, and C.-W. Qiu, Multidimensional nanoscopic chiroptics, Nat. Rev. Phys. **4**, 113 (2022).

[9] J. K. Gansel, M. Thiel, M. S. Rill, M. Decker, K. Bade, V. Saile, G. von Freymann, S. Linden, and M. Wegener, Gold helix photonic metamaterial as broadband circular polarizer, Science **325**, 1513 (2009).

[10] E. Plum, V. A. Fedotov, and N. I. Zheludev, Optical activity in extrinsically chiral metamaterial, Appl. Phys. Lett. **93**, 191911 (2008).

[11] Y. Zhao, M. A. Belkin, and A. Alù, Twisted optical metamaterials for planarized ultrathin broadband circular polarizers, Nat. Commun. **3**, 870 (2012).

[12] W. Li, Z. J. Coppens, L. V. Besteiro, W. Wang, A. O. Govorov, and J. Valentine, Circularly polarized light detection with hot electrons in chiral plasmonic metamaterials, Nat. Commun. **6**, 8379 (2015).

[13] S. Yang, Z. Liu, H. Yang, A. Jin, S. Zhang, J. Li, and C. Gu, Intrinsic chirality and multispectral spin-selective transmission in folded eta-shaped metamaterials, Adv. Opt. Mater. **8**, 1901448 (2020).

[14] T. Shi, Z.-L. Deng, G. Geng, X. Zeng, Y. Zeng, G. Hu, A. Overvig, J. Li, C.-W. Qiu, A. Alù *et al.*, Planar chiral metasurfaces with maximal and tunable chiroptical response driven by bound states in the continuum, Nat. Commun. **13**, 4111 (2022).

[15] A. Basiri, X. Chen, J. Bai, P. Amrollahi, J. Carpenter, Z. Holman, C. Wang, and Y. Yao, Nature-inspired chiral metasurfaces for circular polarization detection and full-Stokes polarimetric measurements, Light: Sci. Appl. **8**, 78 (2019).

[16] M. V. Gorkunov, A. A. Antonov, and Y. S. Kivshar, Metasurfaces with maximum chirality empowered by bound states in the continuum, Phys. Rev. Lett. **125**, 093903 (2020).

[17] V. A. Fedotov, P. L. Mladyonov, S. L. Prosvirnin, A. V. Rogacheva, Y. Chen, and N. I. Zheludev, Asymmetric propagation of electromagnetic waves through a planar chiral structure, Phys. Rev. Lett. **97**, 167401 (2006).

[18] S. Wang, Z.-L. Deng, Y. Wang, Q. Zhou, X. Wang, Y. Cao, B.-O. Guan, S. Xiao, and X. Li, Arbitrary polarization conversion dichroism metasurfaces for all-in-one full Poincaré sphere polarizers, Light: Sci. Appl. **10**, 24 (2021).

[19] E. Plum, X. X. Liu, V. A. Fedotov, Y. Chen, D. P. Tsai, and N. I. Zheludev, Metamaterials: Optical activity without chirality, Phys. Rev. Lett. **102**, 113902 (2009).

[20] W. Chen, Q. Yang, Y. Chen, and W. Liu, Extremize optical chiralities through polarization singularities, Phys. Rev. Lett. **126**, 253901 (2021).

[21] Y. Hou, M. Qiu, Z. Cao, J. Zhou, H. C. Ong, W. Jin, J. Du, and D. Lei, High-Q circular dichroism resonances in plasmonic lattices with chiral unit cells, Adv. Funct. Mater. **32**, 2204095 (2022).

[22] Y. Chen, C. Zhao, Y. Zhang, and C.-W. Qiu, Integrated molar chiral sensing based on high-Q metasurface, Nano Lett. **20**, 8696 (2020).

[23] J. Li and L. Ye, Dielectric dual-dimer metasurface for enhanced mid-infrared chiral sensing under both excitation modes, Nanophotonics **12**, 2189 (2023).

[24] S. Chen, F. Zeuner, M. Weismann, B. Reineke, G. Li, V. K. Valev, K. W. Cheah, N. C. Panoiu, T. Zentgraf, and S. Zhang, Giant nonlinear optical activity of achiral origin in planar metasurfaces with quadratic and cubic nonlinearities, Adv. Mater. **28**, 2992 (2016).

[25] Y. Jiang, W. Liu, Z. Li, D.-Y. Choi, Y. Zhang, H. Cheng, J. Tian, and S. Chen, Linear and nonlinear optical field manipulations with multifunctional chiral coding metasurfaces, Adv. Opt. Mater. **11**, 2202186 (2023).

[26] K. Koshelev, Y. Tang, Z. Hu, I. I. Kravchenko, G. Li, and Y. Kivshar, Resonant chiral effects in nonlinear dielectric metasurfaces, ACS Photon. **10**, 298 (2023).

[27] L. Kang, Y. Wu, and D. H. Werner, Nonlinear chiral metasurfaces based on the optical Kerr effect, Adv. Opt. Mater. **11**, 2202658 (2023).

[28] J. Dixon, M. Lawrence, D. R. Barton, III, and J. Dionne, Self-isolated Raman lasing with a chiral dielectric metasurface, Phys. Rev. Lett. **126**, 123201 (2021).

[29] X. Zhang, Y. Liu, J. Han, Y. Kivshar, and Q. Song, Chiral emission from resonant metasurfaces, Science **377**, 1215 (2022).

[30] A. Overvig, N. Yu, and A. Alù, Chiral quasi-bound states in the continuum, Phys. Rev. Lett. **126**, 073001 (2021).

[31] W. Liu, B. Wang, Y. Zhang, J. Wang, M. Zhao, F. Guan, X. Liu, L. Shi, and J. Zi, Circularly polarized states spawning from bound states in the continuum, Phys. Rev. Lett. **123**, 116104 (2019).

[32] Y. Tang, Y. Liang, J. Yao, M. K. Chen, S. Lin, Z. Wang, J. Zhang, X. G. Huang, C. Yu, and D. P. Tsai, Chiral bound states in the continuum in plasmonic metasurfaces, Laser Photon. Rev. **17**, 2200597 (2023).

[33] J. Von Neuman and E. Wigner, Über merkwürdige diskrete Eigenwerte, On some peculiar discrete eigenvalues, Phys. Z. **30**, 465 (1929).

[34] C. W. Hsu, B. Zhen, J. Lee, S.-L. Chua, S. G. Johnson, J. D. Joannopoulos, and M. Soljačić, Observation of trapped light within the radiation continuum, Nature (London) **499**, 188 (2013).

[35] C. W. Hsu, B. Zhen, A. D. Stone, J. D. Joannopoulos, and M. Soljačić, Bound states in the continuum, Nat. Rev. Mater. **1**, 16048 (2016).

[36] Y. Yang, Y.-P. Wang, J. W. Rao, Y. S. Gui, B. M. Yao, W. Lu, and C.-M. Hu, Unconventional singularity in anti-parity-time symmetric cavity magnonics, Phys. Rev. Lett. **125**, 147202 (2020).

[37] K. Koshelev, S. Lepeshov, M. Liu, A. Bogdanov, and Y. Kivshar, Asymmetric metasurfaces with high-Q resonances governed by bound states in the continuum, Phys. Rev. Lett. **121**, 193903 (2018).

[38] M. V. Rybin, K. L. Koshelev, Z. F. Sadrieva, K. B. Samusev, A. A. Bogdanov, M. F. Limonov, and Y. S. Kivshar, High-Q supercavity modes in subwavelength dielectric resonators, Phys. Rev. Lett. **119**, 243901 (2017).

[39] M. Rybin and Y. Kivshar, Supercavity lasing, Nature (London) **541**, 164 (2017).

[40] N. Bernhardt, K. Koshelev, S. J. U. White, K. W. C. Meng, J. E. Froch, S. Kim, T. T. Tran, D.-Y. Choi, Y. Kivshar, and A. S. Solntsev, Quasi-BIC resonant enhancement of second-harmonic generation in WS_2 monolayers, Nano Lett. **20**, 5309 (2020).

[41] Q.-K. Liu, X.-Q. Luo, X. Xu, Y. Li, W. Zhu, Z. Chen, W. M. Liu, and X.-L. Wang, Interplay of bound states in the continuum empowers spectral-lineshape manipulation in all-dielectric metasurfaces, Phys. Rev. B **107**, 205422 (2023).

[42] K.-H. Kim and J.-R. Kim, High-Q chiroptical resonances by quasi-bound states in the continuum in dielectric metasurfaces with simultaneously broken in-plane inversion and mirror symmetries, Adv. Opt. Mater. **9**, 2101162 (2021).

[43] M. V. Gorkunov, A. A. Antonov, V. R. Tuz, A. S. Kupriianov, and Y. S. Kivshar, Bound states in the continuum underpin near-lossless maximum chirality in dielectric metasurfaces, Adv. Opt. Mater. **9**, 2100797 (2021).

[44] D. F. Edwards, *Handbook of Optical Constants of Solids* (Academic Press, New York, 1997), pp. 547–569.

[45] C. Schinke, P. Christian Peest, J. Schmidt, R. Brendel, K. Bothe, M. R. Vogt, I. Kröger, S. Winter, A. Schirmacher, S. Lim *et al.*, Uncertainty analysis for the coefficient of band-to-band absorption of crystalline silicon, AIP Adv. **5**, 067168 (2015).

[46] K. Koshelev, G. Favraud, A. Bogdanov, Y. Kivshar, and A. Fratalocchi, Nonradiating photonics with resonant dielectric nanostructures, Nanophotonics **8**, 725 (2019).

[47] H. M. Doeleman, F. Monticone, W. den Hollander, A. Alù, and A. F. Koenderink, Experimental observation of a polarization vortex at an optical bound state in the continuum, Nat. Photon. **12**, 397 (2018).

[48] A. A. Basharin, V. Chuguevsky, N. Volsky, M. Kafesaki, and E. N. Economou, Extremely high Q-factor metamaterials due to anapole excitation, Phys. Rev. B **95**, 035104 (2017).

[49] M. Wuttig and N. Yamada, Phase-change materials for rewriteable data storage, Nat. Mater. **6**, 824 (2007).

[50] M. Wuttig, H. Bhaskaran, and T. Taubner, Phase-change materials for non-volatile photonic applications, Nat. Photon. **11**, 465 (2017).

[51] Q. Wang, E. T. F. Rogers, B. Gholipour, C.-M. Wang, G. Yuan, J. Teng, and N. I. Zheludev, Optically reconfigurable metasurfaces and photonic devices based on phase change materials, Nat. Photon. **10**, 60 (2016).

[52] Z. Zhu, P. G. Evans, R. F. Haglund, Jr., and J. G. Valentine, Dynamically reconfigurable metadevice employing nanostructured phase-change materials, Nano Lett. **17**, 4881 (2017).

[53] F. Ding, Y. Yang, and S. I. Bozhevolnyi, Dynamic metasurfaces using phase-change chalcogenides, Adv. Opt. Mater. **7**, 1801709 (2019).

[54] Z. Khan, P. Singh, S. A. Ansari, S. R. Manippady, A. Jaiswal, and M. Saxena, VO_2 nanostructures for batteries and supercapacitors: A review, Small **17**, 2006651 (2021).

[55] A. Tripathi, J. John, S. Kruk, Z. Zhang, H. S. Nguyen, L. Berguiga, P. Rojo Romeo, R. Orobtchouk, S. Ramanathan, Y. Kivshar *et al.*, Tunable Mie-resonant dielectric metasurfaces based on VO_2 phase-transition materials, ACS Photon. **8**, 1206 (2021).

[56] A. V. Kondratov, M. V. Gorkunov, A. N. Darinskii, R. V. Gainutdinov, O. Y. Rogov, A. A. Ezhov, and V. V. Artemov, Extreme optical chirality of plasmonic nanohole arrays due to chiral Fano resonance, Phys. Rev. B **93**, 195418 (2016).

[57] M. L. Solomon, J. Hu, M. Lawrence, A. García-Etxarri, and J. A. Dionne, Enantiospecific optical enhancement of chiral sensing and separation with dielectric metasurfaces, ACS Photon. **6**, 43 (2019).

[58] H. Barkaoui, K. Du, Y. Chen, S. Xiao, and Q. Song, Merged bound states in the continuum for giant superchiral field and chiral mode splitting, Phys. Rev. B **107**, 045305 (2023).

[59] D. V. Bochek, N. S. Solodovchenko, D. A. Yavsin, A. B. Pevtsov, K. B. Samusev, and M. F. Limonov, Bound states in the continuum versus material losses: $Ge_2Sb_2Te_5$ as an example, Phys. Rev. B **105**, 165425 (2022).

[60] Y. Zhang, C. Fowler, J. Liang, B. Azhar, M. Y. Shalaginov, S. Deckoff-Jones, S. An, J. B. Chou, C. M. Roberts, V. Liberman *et al.*, Electrically reconfigurable non-volatile metasurface using low-loss optical phase-change material, Nat. Nanotechnol. **16**, 661 (2021).

[61] L. Kang, R. P. Jenkins, and D. H. Werner, Recent progress in active optical metasurfaces, Adv. Opt. Mater. **7**, 1801813 (2019).

[62] P. C. Wu, C. Y. Liao, V. Savinov, T. L. Chung, W. T. Chen, Y.-W. Huang, P. R. Wu, Y.-H. Chen, A.-Q. Liu, N. I. Zheludev *et al.*, Optical anapole metamaterial, ACS Nano **12**, 1920 (2018).